In vivo longitudinal 920 nm two-photon intravital kidney imaging of a dynamic 2,8-DHA crystal formation and tubular deterioration in the adenine-induced chronic kidney disease mouse model

JIEUN CHOI,[1,2,†] MIN-SUN CHOI,[3,4,†] JEHWI JEON,[1,2] JIEUN MOON,[2,5] JINGU LEE,[2,5] EUNJI KONG,[1,2] (iD) STEPHANI EDWINA LUCIA,[1,2] (iD) SUJUNG HONG,[2,5] JI-HYE LEE,[6] EUN YOUNG LEE,[3,4,7,8] AND PILHAN KIM[1,2,5,*] (iD)

[1]*Graduate School of Medical Science and Engineering, Korea Advanced Institute of Science and Technology (KAIST), Daejeon, 34141, Republic of Korea*
[2]*KI for Health Science and Technology (KIHST), Korea Advanced Institute of Science and Technology (KAIST), Daejeon, 34141, Republic of Korea*
[3]*Department of Internal Medicine, Soonchunhyang University Cheonan Hospital, Cheonan, 31151, Republic of Korea*
[4]*BK21 Four Project, College of Medicine, Soonchunhyang University, Cheonan, 31151, Republic of Korea*
[5]*Graduate School of Nanoscience and Technology, Korea Advanced Institute of Science and Technology (KAIST), Daejeon, 34141, Republic of Korea*
[6]*Department of Pathology, Soonchunhyang University Cheonan Hospital, Cheonan, 31151, Republic of Korea*
[7]*Institute of Tissue Regeneration, College of Medicine, Soonchunhyang University, Cheonan, 31151, Republic of Korea*
[8]*eylee@sch.ac.kr*
[†]These authors contributed equally to this work.
[*]*pilhan.kim@kaist.ac.kr*

Abstract: Chronic kidney disease (CKD) is one of the most common renal diseases manifested by gradual loss of kidney function with no symptoms in the early stage. The underlying mechanism in the pathogenesis of CKD with various causes such as high blood pressure, diabetes, high cholesterol, and kidney infection is not well understood. *In vivo* longitudinal repetitive cellular-level observation of the kidney of the CKD animal model can provide novel insights to diagnose and treat the CKD by visualizing the dynamically changing pathophysiology of CKD with its progression over time. In this study, using two-photon intravital microscopy with a single 920 nm fixed-wavelength fs-pulsed laser, we longitudinally and repetitively observed the kidney of an adenine diet-induced CKD mouse model for 30 days. Interestingly, we could successfully visualize the 2,8-dihydroxyadenine (2,8-DHA) crystal formation with a second-harmonics generation (SHG) signal and the morphological deterioration of renal tubules with autofluorescence using a single 920 nm two-photon excitation. The longitudinal *in vivo* two-photon imaging results of increasing 2,8-DHA crystals and decreasing tubular area ratio visualized by SHG and autofluorescence signal, respectively, were highly correlated with the CKD progression monitored by a blood test showing increased cystatin C and blood urea nitrogen (BUN) levels over time. This result suggests the potential of label-free second-harmonics generation crystal imaging as a novel optical technique for *in vivo* CKD progression monitoring.

1.   Introduction

Chronic kidney disease (CKD) is a long-term disorder characterized by progressive kidney dysfunction in blood pressure, homeostasis, and waste excretion [1]. CKD patient is continuously increasing in the aging population with various risk factors of hypertension, cardiovascular diseases, diabetes, high cholesterol, and genetic alternations [2–4]. The initial nephron damage causes a reduction of renal function that induces additional damage to neighboring nephrons, then can proceed to irreversible renal dysfunction with no noticeable symptoms until the late stage [5]. This vicious cycle emphasizes the significance of early diagnosis and prompt treatment of CKD, suggested by multiple reports on CKD pathophysiology [3,6–10]. However, due to the complexity of etiology, current understanding of the disease mechanism of CKD is quite limited. To obtain a novel clue to diagnose the CKD in early stage and treat the CKD more effectively, a detailed cellular-level analysis of the underlying mechanism of CKD using preclinical animal models is imperative. Toward this end, a direct in vivo longitudinal cellular-level observation of the kidney during the development of CKD in a live animal model is highly desired.

There are various methods to induce CKD in the animal model such as cisplatin nephrotoxicity, adenine supplement, aristolochic acid nephropathy, and 5/6 nephrectomy [11,12]. Among them, an adenine diet-induced CKD mouse model exhibits distinct characteristics of human CKD patients with renal filtration failure accompanied by cardiovascular symptoms [13]. Moreover, the formation of 2,8-dihydroxyadenine (2,8-DHA) crystals in the kidney was found in both the adenine-induced CKD mouse model and human patients with adenine phosphoribosyl transferase deficiency, which is a genetically inherited autosomal recessive disorder [11,12,14]. Until now the adenine-induced CKD model has only been imaged *ex vivo*, and little is known about the *in vivo* pathogenesis of the CKD by excessive adenine and 2,8-DHA crystal accumulation [12].

Herein, we successfully performed a longitudinal repeated intravital two-photon kidney imaging in the mouse model of CKD induced by the adenine diet for 30 days. Notably, a fixed-wavelength 920 nm fs-pulsed laser generated a second harmonics generation (SHG) signal from the 2,8-DHA crystal and autofluorescence signal from renal tubules *in vivo*. Thereby it enabled a direct label-free *in vivo* visualization of the 2,8-DHA crystal formation and morphological change of renal tubules with CKD progression. Pathological kidney changes with increased 2,8-DHA crystal deposition and tubular fragmentation were longitudinally visualized and quantified by repetitive two-photon z-stack imaging of the kidney of the adenine -induced CKD model over time. Furthermore, the imaging results show a high correlation with the deteriorating renal function assessed by a standard clinical blood test of cystatin C and blood urea nitrogen (BUN) levels [11]. Collectively, the CKD progression correlated with the accumulation of the 2,8-DHA crystals could be successfully visualized and monitored by the SHG signal with the longitudinal two-photon intravital kidney imaging.

2.   Methods

2.1.   Animal model

All animal experiments were performed in accordance with the standard guidelines for the care and use of laboratory animals and were approved by the Korea Advanced Institute of Science and Technology Institutional Animal Care and Use Committee (KAIST IACUC, approval no. KA-2021-058). All surgical procedures were done under anesthesia, and all efforts were made to minimize the suffering of animals. C57BL/6N mice were purchased from OrientBio (Suwon, Korea). NG2-DsRed (Jackson Laboratory, Stock No. 008241) [15], CSF1R-GFP (Jackson Laboratory, Stock No. 018549) [16], and CX3CR1-GFP (Jackson Laboratory, Stock No. 005582) [17] mice were purchased from the Jackson Laboratory (Bar Harbor, USA). Aldh1l1-GFP mice (Jackson Laboratory, Stock No. 026033) [18] were generously provided by Dr. Chung at KAIST. All mice were housed and bred in an institutional animal facility in KAIST. They were maintained

in independently ventilated, temperature & humidity-controlled cages (22.5 °C, 52.5%) under 12/12 hours light/dark cycle and provided with a standard diet and water ad libitum. CKD was induced in 7 weeks old C57BL/6N male mice by a 0.2% adenine diet (Envigo, Indianapolis, Indiana, USA) for 30 days [12]. The control group of mice received a regular diet for the same period.

2.2. Kidney histopathology

The kidney tissues were fixed using a 4% paraformaldehyde solution. After fixation, the tissues were embedded in paraffin and sectioned to a thickness of 3 μm for Periodic acid-Schiff (PAS) staining. In addition, 10 μm thickness cryo-sectioned slices were prepared to preserve 2,8-DHA crystal for histological observation. Histological images were obtained under a Leica DMi8 microscope (Leica, Wetzlar, Germany).

2.3. Evaluation of Cystatin C and BUN

Kidney function was monitored by the Cystatin C and blood urea nitrogen (BUN) level. Blood was sampled using capillary on retro-orbital plexus on days 0, 10, 20, and 30 [19]. Cystatin C level was analyzed with a mouse Cystatin C ELISA kit (Biovendor R&D, Brno, Czech Republic). BUN level was assessed with NCal International Standard Kit (Arbor Assays, Ann Arbor, Michigan, USA).

2.4. Intravital imaging system

Commercial intravital two-photon microscope (IVM-MS, IVIM Technology Inc., Daejeon, Korea) was used to visualize the kidney *in vivo*. It integrated a 920 nm fixed-wavelength fs-pulsed laser (Axon-920; Coherent, Santa Clara, CA, USA) with >100:1 linear polarization into a single box, which was used as a two-photon excitation light source for simultaneous SHG and fluorescence imaging. A high numerical aperture (NA) water-immersion objective lens (CFI75 Apochromat 25XC W, NA1.1, Nikon, Tokyo, Japan) was used, which provided an imaging field of view of 447×447 μm^2. The average laser power on the kidney surface was adjusted in the range of 30 mW to 80 mW. Higher power was used at the later time point due to the thickening of kidney capsule and fibrosis with CKD progression. Images were acquired at frame rate of 15 Hz with 1024×1024 pixels (0.437 μm/pixel). Autofluorescence was detected by two NDD detectors equipped with bandpass filters with transmission at 502.5-537.5 nm and 574.0-626.0 nm, respectively. Second harmonics generation (SHG) signal from 2,8-DHA crystal was simultaneously detected by an additional NDD detector equipped with a bandpass filter with transmission at 458.0-463.5 nm.

2.5. Intravital imaging of kidney

Mice were anesthetized using an intramuscular injection of a mixture of Zoletil (20 mg/kg) and Xylazine (11 mg/kg). The abdominal hair of the left-back area was removed using a clipper and a hair removal cream. A 15 mm incision was performed on both the skin and the retroperitoneum and then the kidney was gently exteriorized with round forceps as shown in Fig. 1(a) following the surgical procedure previously described [20]. As shown in Fig. 1(b), wet gauze soaked in warm saline was placed between the kidney and the underlying tissue to reduce motion artifact [21–23]. Warm saline was continuously applied to the gauze during the imaging to avoid dehydration of the exposed visceral surface. During the intravital imaging, the anesthesia level was regularly checked by pinching the mouse's toe. When any response to the pinching was observed, a half of the initial dose of Zoletil and Xylazine mixture was given intraperitoneally. Thirty sequential Z-stack images with 3 μm interval were obtained in the outer renal cortex at more than five randomly selected locations in the kidney to quantify the 2,8-DHA crystal accumulation and tubular structural changes by SHG signal and autofluorescence, respectively. Each Z-stack image

was generated by averaging 30 frames recorded for 2 seconds. The overall image acquisition process took approximately 15 minutes to complete at each time point. In addition, vascular endothelial cells were fluorescently labeled *in vivo* by intravenous injection of Lectin DyLight 488 (DL-1174, Vector Laboratories, CA, USA) at 10 minutes before the intravital imaging. Sodium hyaluronate-carboxymethylcellulose (Guardix, Hanmi, Seoul, Korea) was applied after the imaging as an anti-adhesion agent to prevent excessive adhesion between the kidney and surrounding tissue. The surgical site was closed by in silk suture and an anti-bacterial ointment (Effexin, Ildong, Seoul, Korea) was applied to prevent infection. To reduce inflammation, a nonsteroidal anti-inflammatory drug (Rimadyl, Zoetis, NJ, USA) was injected intraperitoneally. The intravital imaging of kidney was repeatedly performed six times on days 0, 2, 5, 10, 20, and 30 in each CKD mouse model.
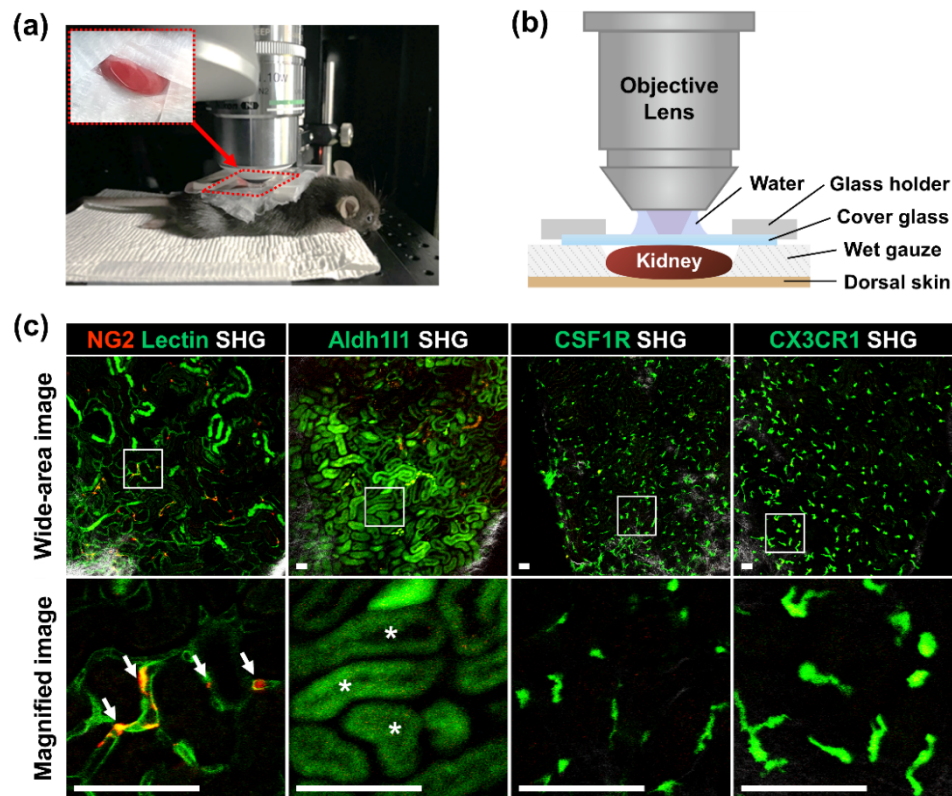

Fig. 1. Intravital two-photon microscopy (TPM) imaging of the kidney of various transgenic reporter mice. (a) Photograph of the preparation of the anesthetized mouse for the intravital kidney imaging. The placement of the exposed kidney is shown in the magnified red dotted box. (b) Cross-sectional diagram of the kidney placement for the intravital kidney imaging. (c) Representative TPM images of the kidney of various transgenic reporter mice, NG2-DsRed, Aldh1l1-GFP, CSF1R-GFP and CX3CR1-GFP mouse. SHG signal (white) from the kidney capsule was visualized. In the NG2-DsRed mouse, blood vessels (green, tomato-lectin) and pericyte (arrow, red, DsRed) were simultaneously imaged. In the Aldh1l1-GFP mouse, tubular epithelial cells (green) in the renal tubules (asterisk) were imaged. In the CSF1R-GFP mouse, myeloid-lineage cells (green) were imaged. In the CX3CR1-GFP mouse, mononuclear phagocytic cells (green) were imaged. Scale bars, 50 μm.

2.6. Imaging analysis and statistical analysis

Image J (National Institutes of Health, Bethesda, MD, USA) was used to automatically identify luminal space tubule area and quantify the intensity of SHG signal [24]. Luminal space area was calculated by measuring the size of empty space over the entire region [25]. At least 18 randomly chosen fields per group were quantified using ImageJ. Tubule abnormal morphology was measured by identifying the change of tubule area of total imaging area over time. Commercial image analysis software, IMARIS (Oxford Instruments, Abingdon, UK), was used to generate three-dimensional volumetric images for quantitative analysis of 2,8-DHA crystal formation. Individual 2,8-DHA crystal was automatically identified and the volume of each crystal was measured using the 'Surface' function of IMARIS. The volumetric ratio of 2,8-DHA crystal in the kidney tissue was calculated by dividing the total volume of 2,8-DHA crystals by the total imaging volume. Origin was used for statistical analysis (OriginLab, Northampton, Massachusetts, USA). For each experimental group (mouse $n \geq 3$), more than five randomly chosen areas were imaged and analyzed. The statistical significance was determined by p-value less than 0.05 with two-tailed unpaired Student's t-test. Pearson correlation coefficients was calculated with Prism (GraphPad, CA, USA).

3. Results

To validate the capability of the *in vivo* cellular-level visualization in the kidney with the procedure described in the Methods section and Fig. 1(a-b), we performed intravital imaging of kidney in various transgenic reporter mice such as NG2-DsRed, Aldh1l1-GFP, CSF1R-GFP and CX3CR1-GFP mice as shown in Fig. 1(c). Second-harmonics generation (SHG) signal based on a nonlinear optical process was observed from the fibrous capsule of the kidney, which was shown at the periphery of the wide area images in Fig. 1(c). In the kidney of NG2-DsRed mouse, blood vessels labeled by intravenously injected tomato lectin and the NG2 + pericytes surrounding the blood vessels (arrows) were simultaneously imaged with green and red fluorescence, respectively [26]. In the kidney of Aldh1l1-GFP mouse, the Aldh1l1 + tubular epithelial cells in the renal tubules (asterisk) were imaged with green fluorescence [27]. In the kidney of CSF1R-GFP mouse, myeloid-lineage cells including monocytes and macrophages expressing green fluorescence were imaged [28]. Similarly, Mononuclear phagocytes such as dendritic cells and macrophages were imaged in the kidney of CX3CR1-GFP mouse [29]. Those imaging results validates the capability of the imaging system for the cellular-level visualization of the kidney of live mouse model.

　Figure 2(a) shows the histological observation of the Periodic acid-Schiff (PAS) stained kidney tissue of control mouse fed a normal diet and adenine diet-induced CKD mouse fed a 0.2% adenine diet for 30 days. The healthy brush-shaped border of epithelial cell has well observed in the renal tubule of the control normal diet mouse. In contrast, the typical tubular morphological changes in CKD such as the epithelium attenuation and the tubular dilatation were observed in the adenine-induced CKD mouse. Hypertrophy of tubule (star) and atrophy of basement membrane (triangle) was observed. Further, the degree of tubular dilation was quantified by measuring the change in the luminal space from day 0 to day 30 as shown in Fig. 2(b). The difference of lumen space in the normal diet model was 11.10 ± 0.95, whereas the adenine diet model had 21.11 ± 1.48 on day 30. The value in the adenine diet model was considerably high with statistical significance ($p < 0.001$). These observations confirmed the successful induction of CKD in the adenine diet fed mouse for 30 days. Interestingly, as shown in Fig. 2(c-d), the 920 nm fs-pulsed laser generated a strong SHG signal from 2,8-dihydroxyadenine (2,8-DHA) crystals identified by light microscopy in the cryo-sectioned kidney slices from the adenine-induced CKD mouse. To note, the 2,8-DHA crystals were reported to be formed in the kidney of the adenine-induced CKD mouse [30,31]. Then, *in vivo* label-free two-photon 3D Z-stack imaging of the kidney of the control normal diet mouse and adenine-induced CKD mouse were performed using the fixed-wavelength 920 nm fs-pulsed laser. SHG signal in 458–463.5 nm, green autofluorescence

at 502-537.5 nm, and red autofluorescence at 574-626 nm were simultaneously imaged *in vivo*. Similar to the imaging results with the cryo-sectioned slices, strong SHG signals from 2,8-DHA crystals were observed in the kidney of adenine-induced CKD mouse *in vivo* as shown in Fig. 2(e). In contrast, no SHG signal was detected from the kidney of the control normal diet mouse while autofluorescence signal was smoothly and uniformly distributed in renal tubules. In the adenine-induced CKD mouse, autofluorescence signal from renal tubules was highly fragmented, which was due to the increased inflammatory lysosome and impaired mitochondrial metabolism [32,33]. To further validate whether the observed optical signal in 458–463.5 nm was mainly generated by two-photon SHG process by 920 nm fs-pulsed laser, the signal intensity from two 2,8-DHA crystals was measured while increasing the average power of the 920 nm fs-pulsed laser on the kidney surface as shown in Fig. 2(d-e). The intensity of the pixels in two 2,8-DHA crystals were quantified using the ImageJ showed a clear linear dependency to squared laser power ($R^2 = 0.974$, square; $R^2 = 0.973$, triangle) as shown in Fig. 2(d), suggesting that they were indeed generated by SHG process [34].

To correlate the *in vivo* longitudinal TPM imaging and CKD progression, we performed a repeated blood test for renal function monitoring and intravital imaging in the same mouse for 30 days ($n \geq 3$, each time point) in two cohorts of control normal diet mouse group and adenine diet-induced CKD mouse group following the experimental scheme shown in Fig. 3(a). blood test for renal function monitoring was performed at 0, 10, 20, and 30 days. Cystatin C and blood urea nitrogen (BUN) levels was measured by using a small amount of blood drawn from the retroorbital cavity with capillary tubes for microhematocrit. After 30 days of adenine diet feeding, the appearance of the kidney changed significantly as shown in Fig. 3(b). The kidneys of adenine-induced CKD mice were smaller and has rough surface in comparison with the kidneys of control normal diet mice, suggesting renal failure and kidney fibrosis. Figure 3(c) shows the difference in the body weight between the control normal diet mice and the adenine-induced CKD mice over time. The mice fed the normal diet gained weight gradually while the adenine diet fed mice exhibited the loss of body weight with statistical significance from day 2 to 30. In normal diet fed mice, both of the cystatin C and BUN levels were stably maintained within a normal range with little changes for 30 days. In contrast, in the adenine-induced CKD mice, both of the cystatin C and BUN levels exhibited a continuous and significant increase until day 20 and then remained at a similar level until day 30 as shown in Fig. 3(d, e). The average cystatin C levels increased by more than two times from 848.76 ± 556.02 ng/ml to 1926.93 ± 399.61 ng/ml. The average BUN increased by approximately 8-fold, from 27.14 ± 5.31 mg/dl to 221.47 ± 15.94 mg/dl, confirming the presence of clinical-level CKD development.

As described before, following the experimental scheme shown in Fig. 3(a), we performed a repeated intravital imaging of kidney and blood test in the same mouse for 30 days ($n \geq 3$, each time point) in two cohorts of control normal diet mouse group and adenine diet-induced CKD mouse group. In each mouse, the intravital TPM imaging was repeatedly performed at 0, 2, 5, 10, 20 and 30 days. Correlated with the longitudinal blood test of stable maintenance of the cystatin C and BUN level within normal range, no significant changes were observed in the kidney of control normal diet mouse by the *in vivo* longitudinal TPM imaging for 30 days. In contrast, in the kidney of adenine-induced CKD mouse, increasing SHG signal by 2,8-DHA crystal formation and gradual deterioration of renal tubules visualized by autofluorescence were clearly imaged as shown in Fig. 4(a). For the volumetric quantification, 3D Z-stack images were obtained at more than 5 randomly selected spot in the kidney of each mouse. Figure 4(b) shows a representative 3D reconstructed SHG image showing the formation of 2,8-DHA crystals with various sizes in the kidney of adenine-induced CKD mouse at day 30. Figure 4(c-d) shows the longitudinal quantification of 2,8-DHA crystal volume ratio and tubular area ratio in the kidney of adenine diet-induced CKD for 30 days. As shown in Fig. 4(a, c), only after 2 days of adenine diet feeding, we could observe an appearance of SHG signal from small 2,8-DHA crystals. The
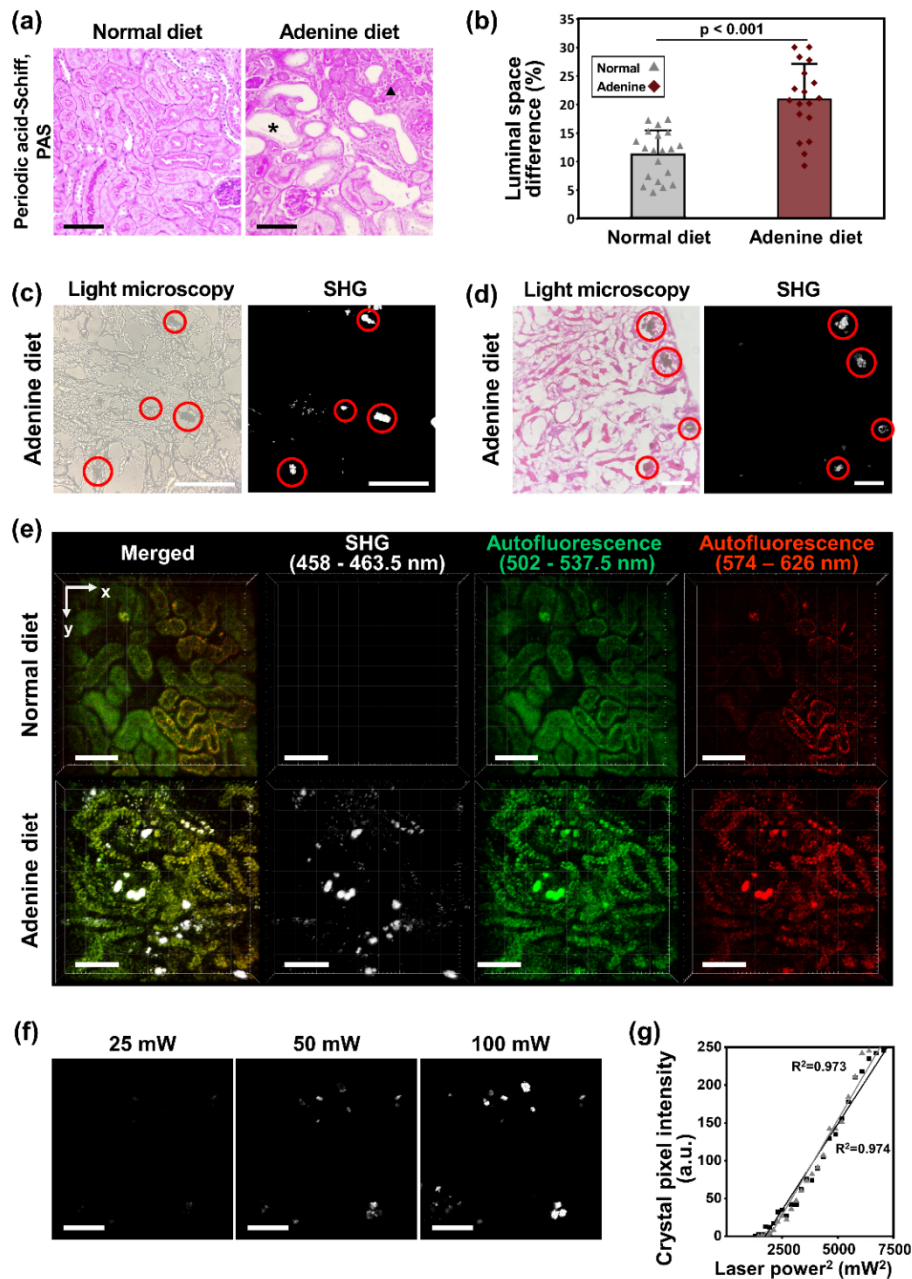
Fig. 2. **Histological and intravital TPM images of the kidney of control normal diet mouse and adenine diet-induced CKD mouse.** (a) Representative *ex vivo* histological images of PAS-stained kidney slice of control normal diet mouse and adenine diet-induced CKD mouse. (b) Quantification of the luminal space differences from day 0 to day 30 ($\geq$ 18 spots per group). All data are presented as mean ± SE of mean, n $\geq$ 3. (c-d) Comparison images of cryo-sectioned kidney slices from adenine diet-induced CKD mouse (c) before or (d) after Eosin staining of stroma. The 2,8-DHA crystals observed by light microscopy or two-photon microscopy for SHG signal detection were marked by red circles. (e) Representative 3D reconstructed intravital TPM images of control normal diet mouse and adenine diet-induced CKD mouse showing 2,8-DHA crystals (SHG, white) and autofluorescence of tubules (green, red). (f) SHG images showing 2,8-DHA crystals while changing the 920 nm fs-pulsed laser powers on kidney surface. (g) Signal intensity of two 2,8-DHA crystals to squared fs-pulsed laser power, showing linear dependency. Scale bars, 100 µm.
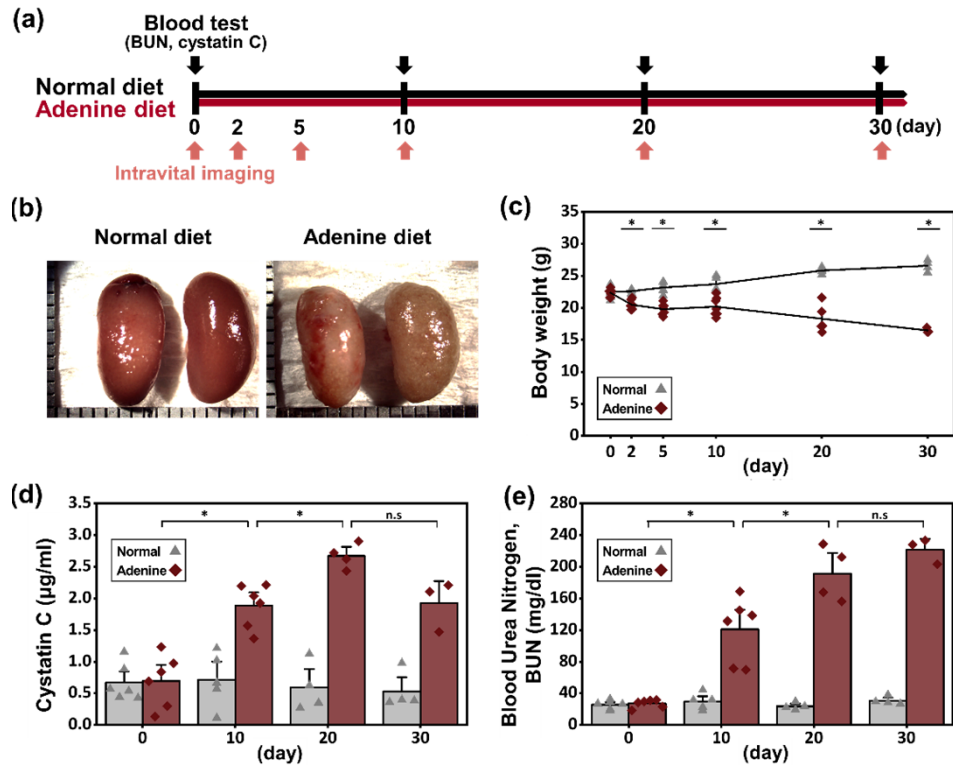
Fig. 3. Longitudinal monitoring of the control normal diet mouse and the adenine diet-induced CKD mouse for 30 days. (a) Experimental scheme of the longitudinal intravital TPM imaging and blood test for 30 days. (b) Representative photograph of the harvested kidneys from the control normal diet mouse and adenine diet-induced CKD mouse at 30 days. (c-e) Quantitative analysis of body weight, cystatin C, and BUN level on day 0, 10, 20, and 30 (n ≥ 3). Data are presented as mean ± SE of mean. Statistical significance was set at *p*-value less than 0.05.

crystal volume ratio gradually and significantly increased from 0% at day 0 to $1.26 \pm 0.18\%$ at day 30. As shown in Fig. 4(a, d), the repetitive autofluorescence imaging successfully captured the morphological tubular deterioration, the increasing fragmentation in the renal tubules and significant decreases in the tubular area ratio from $14.73 \pm 0.75\%$ at day 0 to only $3.52 \pm 0.46\%$ at 30. Finally, the correlations between the longitudinal imaging results of 2,8-DHA crystal volume ratio and tubular area ratio and the blood test results of cystatin C and BUN level were analyzed by the Pearson correlation coefficient (Fig. 4(e, f)). The Pearson coefficients of 2,8-DHA crystal volume ratio was 0.95 for cystatin C level and 0.76 for BUN levels, respectively. And Pearson coefficients of tubular area ratio was -0.92 for cystatin C level and -0.73 for BUN levels, respectively. Both of the 2,8-DHA crystal volume ratio measured by SHG image and the tubular area ratio measured by autofluorescence image demonstrated a strong correlation with the blood tests, particularly with the cystatin C level.
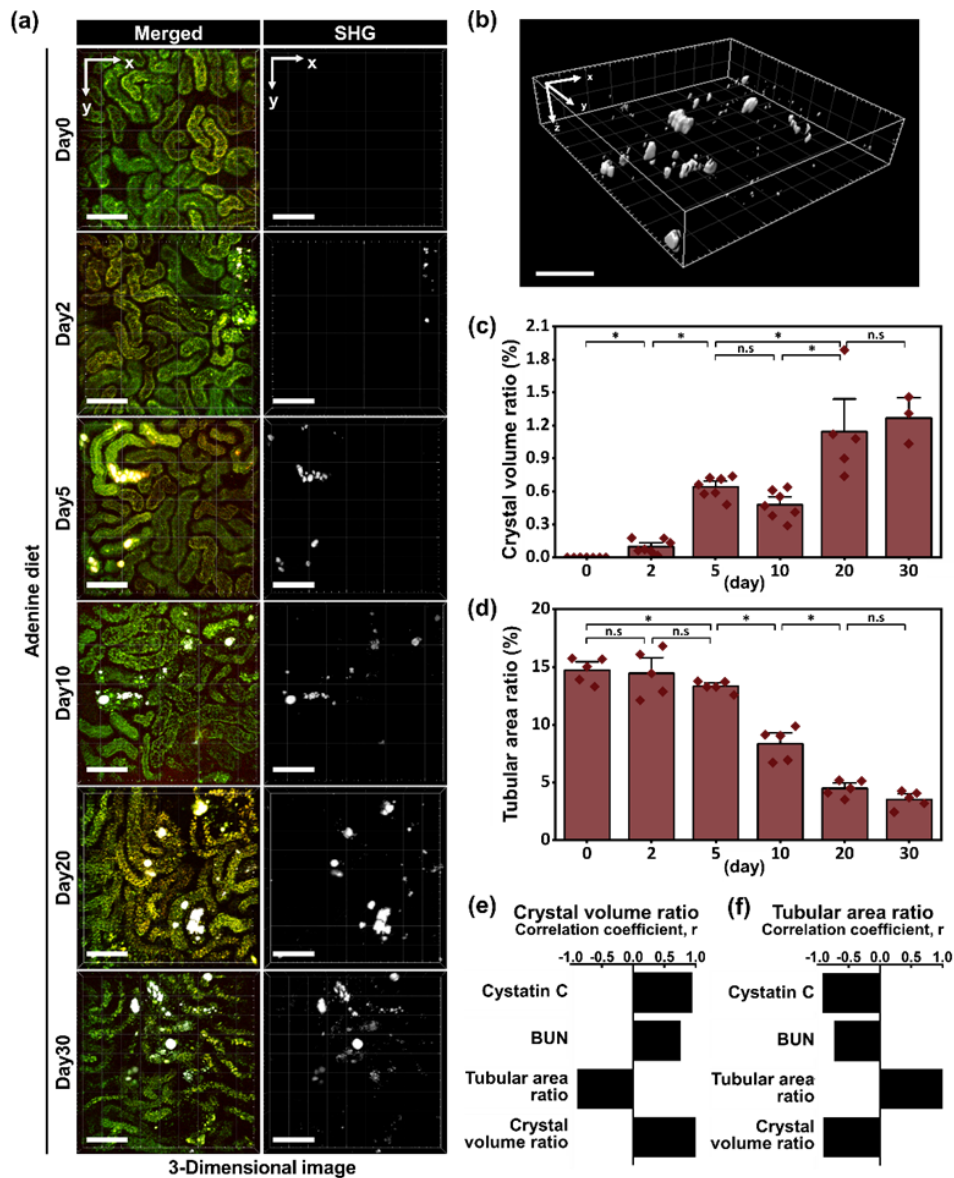
Fig. 4. Longitudinal intravital TPM imaging of the control normal diet mouse and the adenine diet-induced CKD mouse for 30 days. (a) Representative 3D reconstructed TPM images of adenine diet-induced CKD mouse. Tubules were imaged by autofluorescence (green, red) and 2,8-DHA crystals were imaged by SHG signal (white). (b) Representative 3D reconstructed volumetric images of accumulated 2,8-DHA crystals at day 30. (c-d) Quantitative analysis of 2,8-DHA crystal volume ratio and tubular area ratio from day 0 to day 30 (mouse n ≥ 3, imaging spots ≥ 5). (e-f) Pearson correlation coefficient of 2,8-DHA crystal volume ratio and tubular area ratio comparing with cystatin C, blood urea nitrogen (BUN), tubular area ratio, and 2,8-DHA crystal volume ratio. Data are presented as mean ± SE of mean. Statistical significance was set at *p*-value less than 0.05. Scale bars, 100 μm.

4.   Discussion

Chronic kidney disease (CKD) is one of the most common kidney disorders in the world. Various optical imaging modalities including photoacoustic imaging, optical coherent tomographic (OCT), confocal laser-scanning microscopy (CLSM), and narrow band imaging (NBI) have been suggested as potential tools for optical biopsy of renal diseases [35]. However, the application of these methods to visualize dynamic process in living renal tissue at the cellular-level resolution has been technically challenging due to low resolution or limited penetrating depth in live renal tissue. Recently, there have been increasing efforts to utilize two-photon microscopy (TPM) to observe renal morphological and functional changes in live preclinical animal models [36–38]. Notably, renal metabolic functions [32,39] and renal fibrosis [40,41] have been imaged and analyzed by label-free TPM with autofluorescence and SHG signal, respectively. In addition, by utilizing fluorescent tracers, single-nephron glomerular filtration rate [42,43] and organic cations transport [44,45] have been assessed by TPM. Clearly, two-photon *in vivo* longitudinal cellular-level observation to monitor changes in specific type of cells in various renal diseases model of wide range of transgenic mice can deepen our understanding of the pathophysiology of renal diseases.

In this study, for the first time to the best of our knowledge, we demonstrated that intravital TPM could also successfully monitor the 2,8-DHA crystal formation in the CKD mouse model *in vivo*. A fixed-wavelength 920 nm fs-pulsed laser efficiently generated the second harmonics generation (SHG) signal from the 2,8-DHA crystal in the kidney tissue of a live anesthetized CKD mouse model *in vivo*. Reportedly, it has been demonstrated that protein crystals such as tetragonal lysozyme crystals in a petri dish after crystallization can be imaged by TPM with SHG signal [46,47]. Additionally, we could simultaneously detect autofluorescence signal from renal tubules with mitochondrial lipoamide dehydrogenase and mitochondrial flavin adenine dinucleotide [32]. Repeated intravital two-photon cellular-level imaging of the kidney in the adenine-induced CKD mouse model was successfully performed for up to 30 days. The degree of crystal growth and tubular metabolism dysfunction could be quantified with 3D rendered Z-stack two-photon images, which showed a high correlation with the degree of the disease progression monitored by standard clinical blood tests of renal function. Together these results demonstrated that the single-wavelength 920 nm two-photon excited label-free SHG and autofluorescence imaging could be utilized to monitor CKD progression with 2,8-DHA crystal accumulation in the kidney over time *in vivo*. Combined with previously reported various optical imaging techniques, this label-free two-photon imaging method can be a useful tool to improve our understanding of the pathophysiology of CKD, which can ultimately lead to CKD diagnosis and treatment.

Disclosures. The authors declare no conflicts of interest.

Data availability. Data underlying the results presented in this paper are not publicly available at this time but may be obtained from the authors upon reasonable request.

References

1. K. U. Eckardt, J. Coresh, O. Devuyst, R. J. Johnson, A. Kottgen, A. S. Levey, and A. Levin, "Evolving importance of kidney disease: from subspecialty to global health burden," Lancet **382**(9887), 158–169 (2013).
2. J. C. Lv and L. X. Zhang, "Prevalence and disease burden of chronic kidney disease," Adv. Exp. Med. Biol. **1165**, 3–15 (2019).
3. P. R. Gajjala, M. Sanati, and J. Jankowski, "Cellular and molecular mechanisms of chronic kidney disease with diabetes mellitus and cardiovascular diseases as its comorbidities," Front. Immunol. **6**, 340 (2015).
4. M. Canadas-Garre, K. Anderson, R. Cappa, R. Skelly, L. J. Smyth, A. J. McKnight, and A. P. Maxwell, "Genetic susceptibility to chronic kidney disease - some more pieces for the heritability puzzle," Front. Genet. **10**, 453 (2019).
5. J. M. Lopez-Novoa, C. Martinez-Salgado, A. B. Rodriguez-Pena, and F. J. Lopez-Hernandez, "Common pathophysiological mechanisms of chronic kidney disease: therapeutic perspectives," Pharmacol. Ther. **128**(1), 61–81 (2010).

6. M. T. Coughlan, G. C. Higgins, and T. V. Nguyen, *et al.*, "Deficiency in apoptosis-inducing factor recapitulates chronic kidney disease via aberrant mitochondrial homeostasis," Diabetes **65**(4), 1085–1098 (2016).
7. G. Glorieux, W. Mullen, F. Duranton, S. Filip, N. Gayrard, H. Husi, E. Schepers, N. Neirynck, J. P. Schanstra, J. Jankowski, H. Mischak, A. Argiles, R. Vanholder, A. Vlahou, and J. Klein, "New insights in molecular mechanisms involved in chronic kidney disease using high-resolution plasma proteome analysis," Nephrol. Dial. Transplant. **30**(11), 1842–1852 (2015).
8. R. Vanholder and Z. A. Massy, "Progress in uremic toxin research: an introduction," Semin. Dial. **22**(4), 321–322 (2009).
9. F. Hildebrandt, "Genetic kidney diseases," Lancet **375**(9722), 1287–1295 (2010).
10. J. Li, M. Shingde, B. J. Nankivell, M. C. Tchan, B. Bose, J. R. Chapman, K. Kable, S. K. Kim, M. Vucak-Dzumhur, G. Wong, and G. K. Rangan, "Adenine phosphoribosyltransferase deficiency: a potentially reversible cause of CKD," Kidney Int. Rep. **4**(8), 1161–1170 (2019).
11. M. Rabe and F. Schaefer, "Non-transgenic mouse models of kidney disease," Nephron **133**(1), 53–61 (2016).
12. B. H. Ali, S. Al-Salam, M. Al Za'abi, M. I. Waly, A. Ramkumar, S. Beegam, I. Al-Lawati, S. A. Adham, and A. Nemmar, "New model for adenine-induced chronic renal failure in mice, and the effect of gum acacia treatment thereon: comparison with rats," J. Pharmacol. Toxicol. Methods **68**(3), 384–393 (2013).
13. V. Diwan, L. Brown, and G. C. Gobe, "Adenine-induced chronic kidney disease in rats," Nephrology **23**(1), 5–11 (2018).
14. R. Verma, M. Niraimathi, P. Prasad, and V. Agrawal, "Dihydroxyadenine crystal-induced nephropathy presenting with rapidly progressive renal failure," Kidney Res. Clin. Pract. **37**(3), 287–291 (2018).
15. X. Q. Zhu, D. E. Bergles, and A. Nishiyama, "NG2 cells generate both oligodendrocytes and gray matter astrocytes," Development **135**(1), 145–157 (2008).
16. R. T. Sasmono, D. Oceandy, J. W. Pollard, W. Tong, P. Pavli, B. J. Wainwright, M. C. Ostrowski, S. R. Himes, and D. A. Hume, "A macrophage colony-stimulating factor receptor-green fluorescent protein transgene is expressed throughout the mononuclear phagocyte system of the mouse," Blood **101**(3), 1155–1163 (2003).
17. S. Jung, J. Aliberti, P. Graemmel, M. J. Sunshine, G. W. Kreutzberg, A. Sher, and D. R. Littman, "Analysis of fractalkine receptor CX(3)CR1 function by targeted deletion and green fluorescent protein reporter gene insertion," Mol. Cell. Biol. **20**(11), 4106–4114 (2000).
18. H. H. Tsai, H. Li, L. C. Fuentealba, A. V. Molofsky, R. Taveira-Marques, H. Zhuang, A. Tenney, A. T. Murnen, S. P. Fancy, F. Merkle, N. Kessaris, A. Alvarez-Buylla, W. D. Richardson, and D. H. Rowitch, "Regional astrocyte allocation regulates CNS synaptogenesis and repair," Science **337**(6092), 358–362 (2012).
19. A. Sharma, B. L. Fish, J. E. Moulder, M. Medhora, J. E. Baker, M. Mader, and E. P. Cohen, "Safety and blood sample volume and quality of a refined retro-orbital bleeding technique in rats using a lateral approach," Lab. Anim. **43**(2), 63–66 (2014).
20. E. M. Lee, I. Park, Y. J. Lee, Y. H. You, J. W. Kim, M. J. Kim, Y. B. Ahn, P. Kim, and S. H. Ko, "Effect of resveratrol treatment on graft revascularization after islet transplantation in streptozotocin-induced diabetic mice," Islets **10**(1), 25–39 (2018).
21. J. Moon, J. Jeon, E. Kong, S. Hong, J. Lee, E. K. Lee, and P. Kim, "Intravital two-photon imaging and quantification of hepatic steatosis and fibrosis in a live small animal model," Biomed. Opt. Express **12**(12), 7918–7927 (2021).
22. J. Moon and P. Kim, "Intravital two-photon imaging of dynamic alteration of hepatic lipid droplets in fasted and refed state," J. Lipid. Atheroscler. **10**(3), 313–321 (2021).
23. J. Moon, E. Kong, J. Lee, J. Jung, E. Kim, S. B. Park, and P. Kim, "Intravital longitudinal imaging of hepatic lipid droplet accumulation in a murine model for nonalcoholic fatty liver disease," Biomed. Opt. Express **11**(9), 5132–5146 (2020).
24. Y. Chen, Q. Yu, and C. B. Xu, "A convenient method for quantifying collagen fibers in atherosclerotic lesions by ImageJ software," Int. J. Clin. Exp. Med. **10**, 14904–14910 (2017).
25. F. Wang, T. Otsuka, K. Takahashi, C. Narui, D. C. Colvin, R. C. Harris, T. Takahashi, and J. C. Gore, "Renal tubular dilation and fibrosis after unilateral ureter obstruction revealed by relaxometry and spin-lock exchange MRI," NMR Biomed. **34**, e4539 (2021).
26. Y. Feng, Y. Wang, L. Li, L. Wu, S. Hoffmann, N. Gretz, and H. P. Hammes, "Gene expression profiling of vasoregression in the retina–involvement of microglial cells," PLoS One **6**(2), e16865 (2011).
27. X. Q. Chen, J. R. He, and H. Y. Wang, "Decreased expression of ALDH1L1 is associated with a poor prognosis in hepatocellular carcinoma," Med. Oncol. **29**(3), 1843–1849 (2012).
28. M. A. Alikhan, C. V. Jones, T. M. Williams, A. G. Beckhouse, A. L. Fletcher, M. M. Kett, S. Sakkal, C. S. Samuel, R. G. Ramsay, J. A. Deane, C. A. Wells, M. H. Little, D. A. Hume, and S. D. Ricardo, "Colony-Stimulating Factor-1 Promotes Kidney Growth and Repair via Alteration of Macrophage Responses," Am. J. Pathol. **179**(3), 1243–1256 (2011).
29. S. von Vietinghoff and C. Kurts, "Regulation and function of CX3CR1 and its ligand CX3CL1 in kidney disease," Cell Tissue Res. **385**(2), 335–344 (2021).
30. C. E. Metzger, E. A. Swallow, and M. R. Allen, "Elevations in Cortical Porosity Occur Prior to Significant Rise in Serum Parathyroid Hormone in Young Female Mice with Adenine-Induced CKD," Calcif Tissue Int. **106**(4), 392–400 (2020).

31. B. M. Klinkhammer, S. Djudjaj, U. Kunter, R. Palsson, V. O. Edvardsson, T. Wiech, M. Thorsteinsdottir, S. Hardarson, O. Foresto-Neto, S. R. Mulay, M. J. Moeller, W. Jahnen-Dechent, J. Floege, H. J. Anders, and P. Boor, "Cellular and Molecular Mechanisms of Kidney Injury in 2,8-Dihydroxyadenine Nephropathy," J. Am. Soc. Nephrol. **31**(4), 799–816 (2020).

32. M. Bugarski, J. R. Martins, D. Haenni, and A. M. Hall, "Multiphoton imaging reveals axial differences in metabolic autofluorescence signals along the kidney proximal tubule," Am. J. Physiol. Renal. Physiol. **315**(6), F1613–F1625 (2018).

33. T. Thome, M. D. Coleman, and T. E. Ryan, "Mitochondrial bioenergetic and proteomic phenotyping reveals organ-specific consequences of chronic kidney disease in mice," Cells **10**(12), 3282 (2021).

34. R. Wang, F. Wang, J. Long, Y. Tao, L. Zhou, H. Fu, Y. Liu, B. Jiao, L. Deng, and W. Xiong, "Polarized second-harmonic generation optical microscopy for laser-directed assembly of ZnO nanowires," Opt. Lett. **44**(17), 4291–4294 (2019).

35. H. T. Khosroshahi, B. Abedi, S. Daneshvar, Y. Sarbaz, and A. Shakeri Bavil, "Future of the renal biopsy: time to change the conventional modality using nanotechnology," Int. J. Biomed. Imaging **2017**, 6141734 (2017).

36. V. Costanzo and M. Costanzo, "Intravital imaging with two-photon microscopy: a look into the kidney," Photonics **9**(5), 294 (2022).

37. S. L. Wu, H. C. Guo, H. Horng, Y. Liu, H. Li, P. Daneshpajouhnejad, A. Rosenberg, C. Albanese, S. Ranjit, P. M. Andrews, M. Levi, Q. G. Tang, and Y. Chen, "Morphological and functional characteristics of aging kidneys based on two-photon microscopy in vivo," J. Biophotonics **13**, e201900246 (2020).

38. Y. Liu and Z. J. Li, "Intravital microscopy imaging of kidney injury and regeneration," Renal Replacement Ther. **7**(1), 23 (2021).

39. A. M. Hall, R. J. Unwin, N. Parker, and M. R. Duchen, "Multiphoton imaging reveals differences in mitochondrial function between nephron segments," J. Am. Soc. Nephrol. **20**(6), 1293–1302 (2009).

40. M. Strupler, M. Hernest, C. Fligny, J. L. Martin, P. L. Tharaux, and M. C. Schanne-Klein, "Second harmonic microscopy to quantify renal interstitial fibrosis and arterial remodeling," J. Biomed. Opt. **13**(5), 054041 (2008).

41. S. Ranjit, E. Dobrinskikh, J. Montford, A. Dvornikov, A. Lehman, D. J. Orlicky, R. Nemenoff, E. Gratton, M. Levi, and S. Furgeson, "Label-free fluorescence lifetime and second harmonic generation imaging microscopy improves quantification of experimental renal fibrosis," Kidney Int. **90**(5), 1123–1128 (2016).

42. J. J. Kang, I. Toma, A. Sipos, F. McCulloch, and J. Peti-Peterdi, "Quantitative imaging of basic functions in renal (patho)physiology," Am. J. Physiol. Renal. Physiol. **291**(2), F495–F502 (2006).

43. V. Costanzo, L. D'Apolito, D. Sardella, A. Iervolino, G. La Manna, G. Capasso, S. Frische, and F. Trepiccione, "Single nephron glomerular filtration rate measured by linescan multiphoton microscopy compared to conventional micropuncture," Pfluegers Arch. **474**(7), 733–741 (2022).

44. M. Horbelt, C. Wotzlaw, T. A. Sutton, B. A. Molitoris, T. Philipp, A. Kribben, J. Fandrey, and F. Pietruck, "Organic cation transport in the rat kidney in vivo visualized by time-resolved two-photon microscopy," Kidney Int. **72**(4), 422–429 (2007).

45. J. S. Engbjerg, V. Costanzo, D. Sardella, L. Bordoni, S. Jakobsen, L. D'Apolito, J. Frokiaer, F. Trepiccione, G. Capasso, and S. Frische, "The Probe for Renal Organic Cation Secretion (4-Dimethylaminostyryl)-N-Methylpyridinium (ASP+)) Shows Amplified Fluorescence by Binding to Albumin and Is Accumulated In Vivo," Mol. Imaging **2022**, 7908357 (2022).

46. P. Padayatti, G. Palczewska, W. Sun, K. Palczewski, and D. Salom, "Imaging of protein crystals with two-photon microscopy," Biochemistry **51**(8), 1625–1637 (2012).

47. Q. D. Cheng, H. Y. Chung, R. Schubert, S. H. Chia, S. Falke, C. N. Mudogo, F. X. Kartner, G. Chang, and C. Betzel, "Protein-crystal detection with a compact multimodal multiphoton microscope," Commun. Biol. **3**(1), 569 (2020).